

Magnetic shielding of a laboratory Hall thruster. II. Experiments

Cite as: J. Appl. Phys. **115**, 043304 (2014); <https://doi.org/10.1063/1.4862314>

Submitted: 17 October 2013 . Accepted: 24 December 2013 . Published Online: 24 January 2014

Richard R. Hofer, Dan M. Goebel, Ioannis G. Mikellides, and Ira Katz



View Online



Export Citation



CrossMark

ARTICLES YOU MAY BE INTERESTED IN

[Magnetic shielding of a laboratory Hall thruster. I. Theory and validation](#)

Journal of Applied Physics **115**, 043303 (2014); <https://doi.org/10.1063/1.4862313>

[Tutorial: Physics and modeling of Hall thrusters](#)

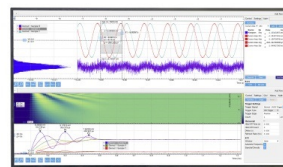
Journal of Applied Physics **121**, 011101 (2017); <https://doi.org/10.1063/1.4972269>

[Magnetic shielding of the channel walls in a Hall plasma accelerator](#)

Physics of Plasmas **18**, 033501 (2011); <https://doi.org/10.1063/1.3551583>

Challenge us.

What are your needs for
periodic signal detection?



Zurich
Instruments



Magnetic shielding of a laboratory Hall thruster. II. Experiments

Richard R. Hofer,^{a)} Dan M. Goebel, Ioannis G. Mikellides, and Ira Katz
Jet Propulsion Laboratory, California Institute of Technology, 4800 Oak Grove Drive, Pasadena, California 91109, USA

(Received 17 October 2013; accepted 24 December 2013; published online 24 January 2014)

The physics of magnetic shielding in Hall thrusters were validated through laboratory experiments demonstrating essentially erosionless, high-performance operation. The magnetic field near the walls of a laboratory Hall thruster was modified to effectively eliminate wall erosion while maintaining the magnetic field topology away from the walls necessary to retain efficient operation. Plasma measurements at the walls validate our understanding of magnetic shielding as derived from the theory. The plasma potential was maintained very near the anode potential, the electron temperature was reduced by a factor of two to three, and the ion current density was reduced by at least a factor of two. Measurements of the carbon backscatter rate, wall geometry, and direct measurement of plasma properties at the wall indicate that the wall erosion rate was reduced by a factor of 1000 relative to the unshielded thruster. These changes effectively eliminate wall erosion as a life limitation in Hall thrusters, enabling a new class of deep-space missions that could not previously be attempted. © 2014 AIP Publishing LLC. [<http://dx.doi.org/10.1063/1.4862314>]

I. INTRODUCTION

Electron transport and channel erosion are two major technical challenges that have persisted since the invention of the Hall thruster over 50 years ago. The first relates to the existence of anomalous cross-field electron current that is necessary to sustain the discharge but also limits performance. While a predictive theory has yet to emerge, methods have been devised to regulate the electron current and achieve high-performance over wide throttling ranges.^{1,2} A second major challenge in Hall thrusters is erosion of the channel walls that limits service life. Sufficient improvement has been made in this area to position Hall thrusters to dominate near-Earth missions in commercial and military applications. However, in the civil space sector, the propellant throughput capabilities have not yet reached sufficiently high levels for Hall thrusters to be widely considered for use on deep-space missions. While this constraint can be mitigated through the use of multiple thrusters, this approach increases the mass and cost of the propulsion system, ultimately limiting the number of applicable missions.

The path towards mitigating channel erosion in Hall thrusters begins with the concept of the thermalized potential, $\phi_0 \approx \phi - T_{e0} \times \ln(n_e/n_{e0})$, which is constant along a magnetic field line if the electrons are also isothermal. Here, ϕ is the plasma potential, T_{e0} is the electron temperature, n_e is the plasma density, and n_{e0} is a reference plasma density usually chosen on channel centerline. The thermalized potential was first discussed in the context of Hall thrusters by Morozov³ in the 1960s. Morozov usually considered the limit of negligible electron temperature $T_e \rightarrow 0$, which leads to the equipotentialization of the magnetic field lines. Indeed, this assumption is implicit in a review of Hall thrusters published in 2000, where Morozov and Savelyev⁴ state: "...at the beginning of the 1960s magnetic-force-line equipotentialization became

known, and the chosen geometry of force lines (convex toward the anode) provided repulsion of ions from the walls by the electric field, thus reducing the channel erosion." Morozov recognized that the electron temperature must be negligibly small in order for the electric (**E**) and magnetic (**B**) field vectors to be orthogonal. However, the problem is that the electron temperature is not negligible in the acceleration zone of a modern Hall thruster. Morozov's realization that convex field lines could influence the electric potential was apropos, but the claim that this structure could repel ions from the walls was never demonstrated sufficiently to retire wall erosion as a failure mode.

Recently, a new technique called "magnetic shielding" was proposed to eliminate channel erosion that was enabled by two major events: (1) Aerojet designed and built the BPT-4000 that demonstrated a zero-erosion state after 5.6 kh of a 10.4 kh qualification test, and (2) the Jet Propulsion Laboratory (JPL) performed numerical simulations of the BPT-4000 that explained the physics behind these test results.⁵⁻⁷ The BPT-4000 simulations also explained why erosion of this thruster in the beginning of the life test occurred at rates observed in other Hall thrusters, and why it stopped after material was eroded away to expose a critical magnetic field topology to the plasma. These explanations led to the development of magnetic shielding theory and laboratory demonstration with a magnetically shielded Hall thruster called the H6MS.⁸⁻¹²

Magnetic shielding recognizes the significance of deviations from "magnetic-force-line equipotentialization," which occur naturally in these devices due to the variation of the electron number density along the lines of force when the electron temperature is finite. Such deviations increase in the acceleration zone where the electron temperature is high and can occur not only inside the wall sheath but also in the pre-sheath and in the bulk plasma. The implication is that a component of the induced electric field along the magnetic field can and usually is established that accelerates beam ions towards the walls

^{a)}Electronic mail: richard.r.hofer@jpl.nasa.gov.

causing erosion. As a result of this breakdown in the orthogonality of the two fields, a geometry of magnetic field lines with convex curvature toward the anode cannot effectively control the electric field near surfaces (and, in turn, the erosion) if the near-wall lines are not also equipotential.

Magnetic shielding seeks to achieve equipotentialization of the lines of force near the walls. By doing so, the plasma potential there can be sustained, in principle, at values that equal (or are near) the discharge voltage. In this manner, the kinetic energy that ions gain through the potential drop in the plasma along surfaces can be eliminated or reduced significantly. We have argued that this can be achieved by taking advantage of the isothermal properties of the lines of force,^{6,11,12} with a magnetic field topology that extends lines adjacent to the walls deep into the anode region where the electrons are cold (<5 eV). In doing so, not only the contribution of the electron pressure to deviations from equipotentiality is marginalized but also the energy that ions gain through the sheath is reduced significantly. This nearly ideal equipotentialization then allows for true control of the electric field by the magnetic field because it preserves their orthogonal properties.

Due to the electrode configuration, the magnetically shielded Hall thruster described here is distinctly different than the so-called “Thruster with Anode Layer” (TAL).^{13,14} The discharge chamber walls in a TAL are metallic and are typically biased to the cathode potential in order to minimize electron energy losses. In a magnetically shielded Hall thruster, the insulating walls are floating near the anode potential due to the magnetic field configuration. Ions reaching the wall of a TAL can attain nearly the entire applied discharge potential resulting in erosion rates that are of the same order as unshielded Hall thrusters. In a magnetically shielded thruster, the ion energy is only a few volts, which results in orders of magnitude lower erosion rates than either an unshielded Hall thruster or a TAL.

In this paper, we validate through experiments the first principles of magnetic shielding in Hall thrusters. The first part of this series described the implementation of the theory through a physics-based design methodology exclusively using numerical simulation.¹² Here, we report on experiments comparing the erosion characteristics of a thruster modified to achieve magnetic shielding. A description of the design modifications and experimental apparatus follow. A multitude of diagnostics were employed to assess the performance, thermal, stability, and wear characteristics of the thruster. Results and discussion from the experiments are then presented. Our results demonstrate that the magnetically shielded thruster configuration reduced the erosion rates relative to its original unshielded configuration by orders of magnitude while maintaining high-performance. We conclude that the experiments validate magnetic shielding theory, paving the way towards the flight of erosionless Hall thrusters in space.

II. EXPERIMENTAL APPARATUS

In the experiments, a series of diagnostics were used to quantify the performance, thermal, stability, and wear

characteristics of a 6 kW laboratory Hall thruster using two distinct thruster configurations. The original or baseline version of the thruster is referred to here as the “unshielded (US) configuration.” The modified version of the thruster is termed the “magnetically shielded (MS) configuration.” The US configuration was the existing one for which a large body of data exists.^{15–21} This configuration provides for high-performance of the thruster, but as will be shown here, is unshielded from ion bombardment, which will limit its propellant throughput capability. The MS configuration was designed using a physics-based methodology in Mikellides *et al.*⁸ to shield the discharge chamber walls from ion bombardment while maintaining high-performance. This article is focused on the discharge chamber probes and erosion diagnostics used to assess the changes in wear rates. Results from the performance, thermal, and stability investigations of Hofer *et al.*¹⁰ will be briefly summarized. Photographs of the experimental configuration are shown in Figure 1. The thruster was mounted to a thrust stand in a large vacuum chamber. In the near-field plume of the thruster, a pair of linear stages provided high-speed radial and axial translation. These stages were used for probing the plasma internal to the discharge chamber and as far as one thruster mean channel diameter (D_m) downstream

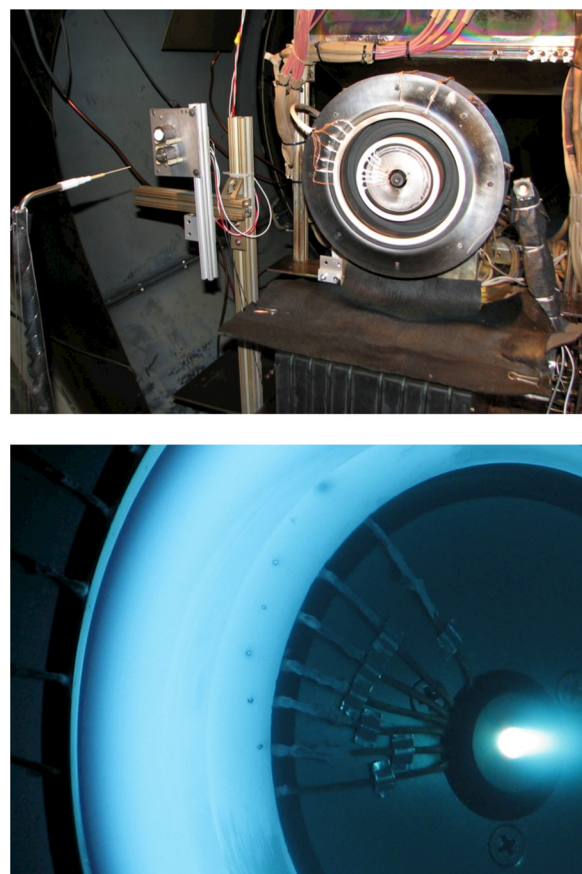


FIG. 1. Photographs of the experimental configuration showing the H6 Hall thruster installed on the thrust stand during wall probe testing. Top: To the left of the thruster, a cylindrical Langmuir probe used for internal discharge chamber measurements is shown. To the right of the thruster, the QCM used for measuring the backscatter rate of carbon is visible. Bottom: Operation of the flush-mounted wall probes in the MS configuration used to measure ion current density, electron temperature, and plasma potential.

of the channel exit plane. The position of the various measurements from the diagnostics are referenced to a radial-axial (r, z) coordinate system with the radial origin at the centerline of the thruster and the axial origin at the downstream face of the anode. Axial positions are normalized to the length of the discharge chamber (L_c) for $z < D_m$.

A. H6 Hall thruster

All experiments were conducted using the H6 Hall thruster. The H6 is a nominally 6 kW laboratory Hall thruster that was developed as a testbed for studies of thruster physics and developments in diagnostics and thruster technology.¹⁵ The thruster was a joint development between JPL, the University of Michigan, and the Air Force Research Laboratory and copies of the thruster continue to be studied at each institute. High-performance is achieved through the use of a plasma lens magnetic field topology,^{1,2,22} a centrally mounted lanthanum hexaboride (LaB_6) cathode,^{19,23} and a high-uniformity gas distributor/anode assembly.¹⁷ The throttling range of the thruster is approximately 0.6–12 kW discharge power, 1000–3000 s specific impulse, and 50–500 mN thrust.

Implementing magnetic-shielding in the H6 required changes to the magnetic circuit and discharge chamber. New pole pieces were fabricated for the magnetic circuit that were exchanged with existing parts. Illustrated in Figure 2, the discharge chamber of the thruster is designed with replaceable boron nitride (BN) rings. These rings have axial lengths that overlap the acceleration zone, such that new parts can be fabricated to accommodate design changes or wall diagnostics.^{24,25} New rings were fabricated for these experiments with geometries compatible with magnetic shielding.

During the experiments, power and propellant were delivered to the H6 with commercially available power supplies and flow controllers. The plasma discharge was sustained by a pair of power supplies wired in parallel capable of up to 500 V, 40 A operation. The discharge filter consisted of an 80 μF capacitor in parallel with the discharge power supply outputs. Xenon was supplied through stainless steel feed lines with 50 and 500 sccm mass flow controllers. The controllers were calibrated before the experiment and were

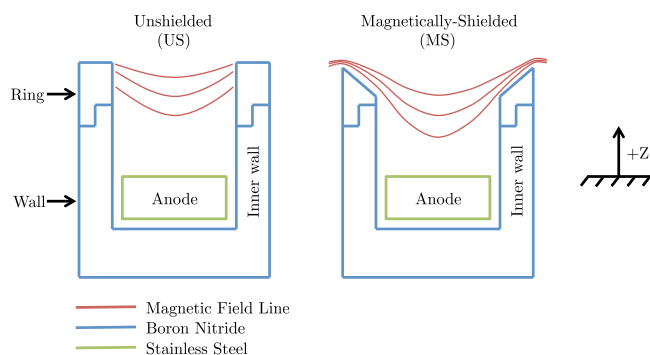


FIG. 2. Schematic illustrating the discharge chamber geometry and notional magnetic field of the US and MS configurations. Between configurations, only the rings and magnetic pole pieces (not shown) are changed. Not to scale.

digitally controlled with an accuracy of $\pm 1\%$ of the set point. The cathode flow rate was always set to 7% of the anode flow rate.

B. Vacuum facility

Experiments were performed in the Owens Chamber at JPL. The 3 m diameter by 10 m long, cryogenically pumped vacuum chamber has been used previously to test gridded ion and Hall thrusters at power levels exceeding 20 kW. Pressure is monitored in the chamber using a pair of ionization gauges and a Residual Gas Analyzer (RGA). The RGA is used to measure the partial pressures of the gases in the facility when the base pressure is reached. The first ionization gauge is calibrated for nitrogen and mounted to the chamber wall downstream of the thruster exit plane. This gauge is used to measure the base pressure of the facility. The second ionization gauge is calibrated for xenon and mounted below the thrust stand. This gauge is used to measure the operating pressure during thruster operation. For these experiments, the base pressure was typically 5×10^{-7} Torr or less. As indicated by the RGA, water vapor was the largest single background gas present, followed by nitrogen, oxygen, and mechanical pump oil. The nitrogen and oxygen partial pressures were as much as a factor of 100 less than the maximum recommended levels in order to avoid significant changes in insulator erosion.^{24,25} At the maximum xenon flow rate of 21.53 mg/s, the operating pressure was 1.6×10^{-5} Torr, equivalent to a pumping speed of 174 kl/s at the standard temperature of 0 °C.

C. Discharge chamber plasma probes

1. Wall probes

An array of flat probes was installed in the discharge chamber wall of the inner and outer rings for both thruster configurations. The approach used techniques similar to those developed by Shastry *et al.*^{24,25} Six 0.5 mm diameter flat tungsten probes were inserted through each of the boron nitride rings and mounted such that the probe surface was flush with the ring surface as shown in Figure 1. In the US configuration, the probes were positioned identical to those chosen by Shastry *et al.*^{24,25} In the MS configuration, similar positions were chosen with the first probe positioned as close to the exit plane as could be achieved without damaging the wall. The probes could have a fixed bias applied for ion saturation current measurements or an applied voltage sweep with a variable amplitude with a duration of 4 ms to measure electron temperature and plasma potential. The uncertainty in the electron temperature, plasma potential, and ion current density is estimated to be $\pm 10\%$, ± 5 V, and $\pm 50\%$, respectively.

2. Internal centerline probes

A fast scanning probe was used to measure the plasma potential and electron temperature on the channel centerline. The emphasis of the present work was on obtaining centerline data over the range of $z/L_c = 0.5$ to 1.8. The probe drive consisted of two Velmex belt-driven bi-slides capable of

peak speeds in vacuum of 0.7 m/s and the dwell time at full insertion before retraction was less than 20 ms. The probe system used two interchangeable tips consisting of a cylindrical Langmuir probe to measure electron temperature and an emissive probe to measure plasma potential.

Electron temperature measurements were obtained using a 0.5 mm diameter, 1.5 mm long cylindrical Langmuir probe encased by a 1.5 mm diameter alumina tube. A thin boron nitride tube 2 mm in diameter was cemented over the alumina to reduce the secondary electron yield and power loading in the high electron temperature regions.²⁶ The probe voltage was swept with a 4 ms, 100 V ramp that was biased relative to a reference potential.²⁷ The reference potential was increased as the probe was inserted deeper into the channel. The data acquisition system sampled the current, voltage, and probe position at 200 kHz per channel, which permitted each current-voltage sweep to contain about 800 points. The electron temperature as a function of axial position was determined from an exponential fit to the data in the electron-repelling region of the trace. The uncertainty in the electron temperature is estimated to be $\pm 10\%$.

The plasma potential profile on the channel centerline was measured by a floating emissive probe. The probe used two 1.5 mm diameter alumina tubes to support 0.5 mm diameter tantalum connection wire that was spot welded to a 0.125 mm diameter tungsten wire that protruded about 2.5 mm from the ends of the ceramic tubes. A thin boron-nitride sleeve was slipped over the alumina tubes to reduce the secondary electron yield to minimize the power deposition on the ceramics during insertion deep into the channel. The filament was heated by a floating heater supply and the probe potential measured relative to ground through a high impedance voltage divider into a 200 kHz data acquisition system. The plasma potential was calculated from the floating probe potential with respect to ground plus the measured cathode-to-ground coupling voltage plus $T_e/2$.²⁸ The uncertainty in the plasma potential is estimated to be ± 5 V.

D. Erosion diagnostics

A Coordinate Measuring Machine (CMM) was used to measure the geometry of the insulator rings before and after testing. Wall profiles were typically obtained at four equally spaced locations around the circumference of a ring and then averaged. The resolution of the CMM with a TP20 probe tip is reported by the manufacturer to be ± 3 μm . Analysis of the various data sets taken in these experiments resulted in a resolution of ± 30 μm . Expressed as an erosion rate for a reference 10 h run time, we estimate the noise floor of the CMM to be ± 1 $\mu\text{m}/\text{h}$.

A Quartz Crystal Microbalance (QCM) was used to measure the backsputter rate of carbon from the surfaces of the vacuum chamber subject to high-energy ion bombardment. The readout of the QCM was used in total deposition mode with the instrument parameters set for carbon. The QCM was water-cooled and the temperature was maintained to less than 1 °C. As shown in Figure 1, the QCM was axially positioned at the exit plane of the thruster discharge chamber and radially positioned within 3 cm of the thruster outer front pole.

The uncertainty of the backsputter rate from the QCM measurements was estimated to be $\pm 1 \times 10^{-3}$ $\mu\text{m}/\text{h}$.

III. RESULTS

Experiments were conducted with the H6 Hall thruster in the US and MS configurations for an operating condition of 300 V, 20 A. Table I lists the various configurations that were tested. The individual experiments are described in terms of the magnetic circuit used, a trial letter, and a segment. The core trials are US-A and MS-A. If the trial letter is not specified, these are the trials that are being discussed. Outside this core, two additional trials were briefly investigated: (1) US-B tested the US magnetic circuit with the insulator rings geometry of the MS configuration and (2) MS-B repeated the same conditions as MS-A. Cumulative operating times are also listed in Table I. For the US-A and MS-A trials, the times correspond to instances where the ring geometry was measured with the CMM.

Core testing in the US configuration established the baseline for comparison when the thruster was later modified to the MS configuration. The US configuration tested the thruster under conditions for which a vast amount of data from prior investigations already exists. However, as it was desired to control variations in the vacuum facility, thruster, and diagnostics as much as possible, new insulator rings were used and all measurements that would also be made in the MS configuration were made during the US configuration experiments. As determined through prior investigations, inner and outer coil currents with the US configuration that corresponded to maximum total thrust efficiency were 3.5 and 3.13 A, respectively.

In the MS configuration, optimization of the magnetic field intensity for peak performance was required as this was the first time the thruster was operated in this manner. Although data were collected at other magnetic field settings, unless specified the inner and outer coils were operated at 4.0 and 3.31 A, respectively. These coil current settings correspond to maximum total efficiency and although operated at higher coil currents than the US configuration, actually correspond to a 20% lower magnetic field intensity due to changes in the magnetic circuit that were introduced for magnetic shielding. All comparisons between the US and MS configurations here are at the same discharge conditions (300 V, 20 A) and at magnetic field intensities yielding maximum total efficiency.

Upon establishing the MS discharge, visual inspection revealed distinct differences in the structure of the plasma in

TABLE I. Description of the various thruster trials executed over the course of the experimental campaign.

| Label-trial-segment | Magnetic circuit | Insulator ring geometry | Cumulative operating time (h) | Profilometry acquired? |
|---------------------|------------------|-------------------------|-------------------------------|------------------------|
| US-A-1 | US | US | 6.98 | Y |
| US-A-2 | US | US | 27.93 | Y |
| US-B-1 | US | MS | 10 | N |
| MS-A | MS | MS | 19.49 | Y |
| MS-B | MS | MS | 14 | N |

the discharge chamber. Photographs of the H6 operating in the US and MS configurations are shown in Figure 3. Whereas the US discharge largely fills the discharge chamber and appears (at least to the human eye) to be in close proximity to the walls, the MS discharge contains a zone of intense emission with noticeable gaps on either side of the channel between the wall and the primary emission zone. Figure 4 is a magnified view of the discharge chamber in the MS configuration highlighting the decreased emission near the walls. In this view, the anode is actually visible through the wall gap. Since we expect magnetic shielding to significantly reduce plasma-wall interactions, these qualitative observations were the first indications that magnetic shielding had likely been achieved in the H6 thruster.

Photographs of the thruster in the MS configuration before and after 15 h of testing are shown in Figure 5. A dark-colored, conductive, thin-film was observed to cover almost the entire surface of the insulator rings. Analysis of these films in the US configuration using energy-dispersive

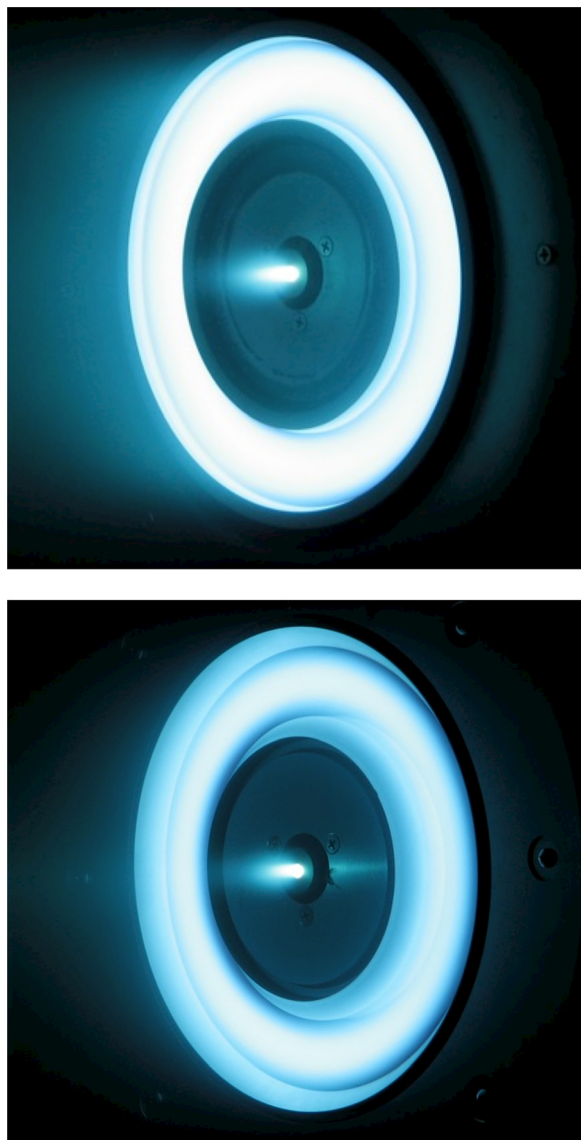


FIG. 3. Operation of the H6 at 300 V, 20 A in the US (top) and MS (bottom) configurations.



FIG. 4. Operation of the H6 in the MS configuration. Intense emission is seen in the bulk of the channel with gaps near the walls. In the photograph, a clear line of sight is visible to the anode in the back of the discharge chamber.

X-ray spectroscopy showed they contain carbon, which likely originated from material backspattered from the carbon panels lining the vacuum chamber wall. Since the carbon backscatter rate was known to be several orders of magnitude lower than the erosion rate of the US configuration, this was the second qualitative observation indicating that magnetic shielding had been achieved.

The performance, stability, and thermal characteristics of the US and MS configurations were also measured but

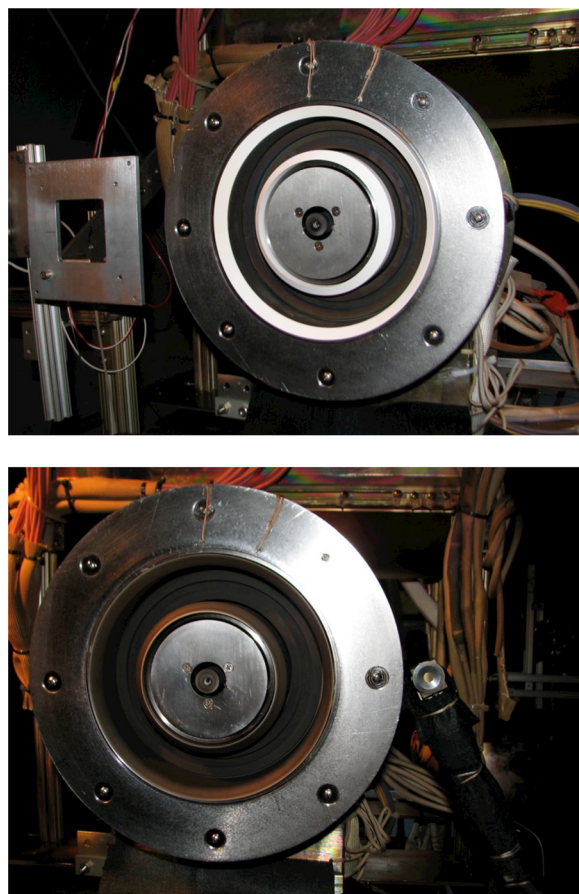


FIG. 5. H6 in the MS configuration installed in the vacuum chamber before (top) and after (bottom) testing. After testing, the boron nitride rings were coated with a film of carbon backspattered from the vacuum chamber walls.

will only be summarized here with additional results given elsewhere.¹⁰ Performance was optimized in the MS configuration by identifying the magnetic field intensity corresponding to maximum total efficiency under conditions of constant anode mass flow rate. Thrust, total specific impulse, and total efficiency in the MS configuration were 384 mN, 2000 s, and 62.4%, respectively. Relative to the US configuration, thrust, total specific impulse, and total efficiency changed by -4.2% , 2.6% , and -1.7% , respectively. Discharge current oscillations increased 25% with the MS configuration to a RMS value of 1.0 A, but otherwise the discharge stability was not significantly effected. The startup behavior is similar in both configurations and both discharges are stable over firings of several hours after reaching thermal equilibrium with the vacuum chamber environment. Discharge current drifts over time in the MS configuration behaved very similarly to the US configuration over hours of operation where only ~ 0.05 A drifts are typically observed. Temperature measurements show a $60\text{--}80^\circ\text{C}$ ($12\%\text{--}16\%$) decrease in the ring temperature for the MS configuration relative to the US configuration. Overall, it was concluded that high-performance was maintained with the MS configuration while maintaining favorable stability and thermal characteristics.

A. Discharge chamber and near-field plasma properties

The wall probes show dramatic differences in the plasma parameters at the wall that are consistent with the theoretical predictions for magnetic shielding.¹² The plasma

potential and electron temperature profiles measured by the wall probes installed on the outer ring of the US configuration are shown in Figure 6 (top left). Nearly identical potential and temperature profiles were found from the probes on the inner ring, as shown in Figure 6 (top right). For the US configuration, the acceleration region is seen to be relatively narrow because the anode potential is reached in less than $z/L_c = 0.2$ upstream of the exit plane. The electron temperature measured on both inner and outer rings peaks at 32 eV, and mapping of the temperature along the magnetic field lines confirms isothermality.¹²

The potential and electron temperature profiles measured by the wall probes in the chamfered rings of the MS configuration are shown in Figure 6 (bottom). The exit plane of the H6MS is $z/L_c = 0.05$ upstream of the exit plane of the H6US, so care must be taken in directly comparing the profiles. It is clear that the plasma parameters along the wall are radically different in the MS configuration. The plasma potentials in the MS configuration on the outer and inner rings were measured to be above the anode potential all along the wall surface. Likewise, the electron temperature is below 10 eV along the outer wall, illustrating the magnetic fields in the magnetically shielded region map directly to the higher potential, lower temperature plasma near the anode.

Nearly identical potential and temperature profiles were found from the probes on the inner wall seen in Figure 6 (bottom right), with the exception that the electron temperature on the farthest downstream probe was 13 eV, which was 3 eV higher than the outer wall. Electron temperatures this high were not predicted,¹² but we have found through subsequent

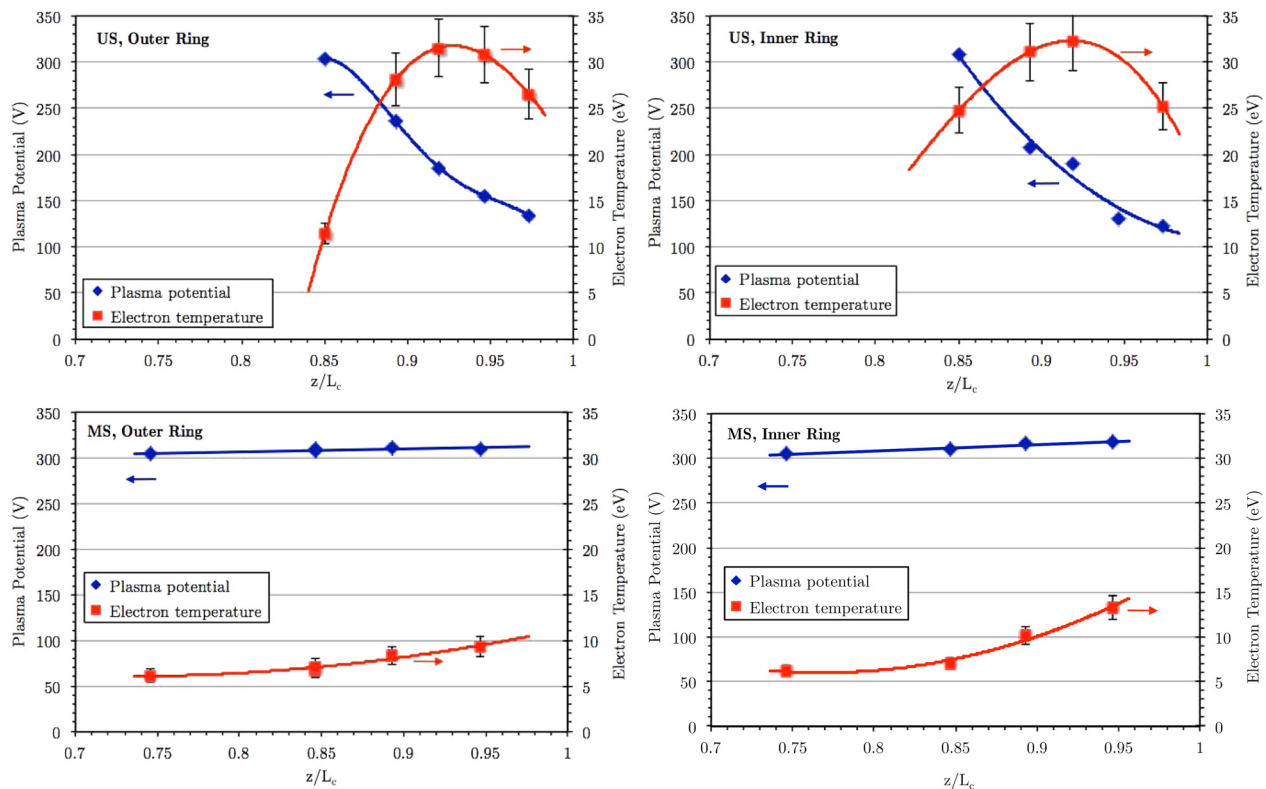


FIG. 6. Plasma potential (relative to cathode) and electron temperature measured by the wall probes for the US (top) and MS (bottom) configurations on the outer (left) and inner (right) rings. Comparison between the configurations demonstrates the effects of magnetic shielding on the plasma parameters at the walls.

testing that if the pole pieces are not precisely assembled, small deviations in the magnetic field topology can affect the plasma properties in this region.⁹ Designing the pole pieces to avoid this possibility is a tractable problem that will be resolved in future thrusters. Other possible sources of this discrepancy are discussed in our companion paper.¹² Regardless of the specific source of the discrepancy, the higher T_e measured by the wall probes than predicted does not alter significantly the effectiveness of magnetic shielding in this region because the major contribution to the erosion, the kinetic energy gained by ions in the plasma, was indeed found to be significantly lower in the MS configuration.

The comparison of the wall probe data for the unshielded and shielded cases in Figure 6 clearly shows the effect of magnetic shielding on the plasma. The plasma potential along the wall in the MS configuration remains near the discharge voltage such that ions from the ionization region upstream of the peak magnetic field (closer to the anode) gain little or no kinetic energy before impacting the wall. Likewise, the electron temperature is relatively low at the wall, so the sheath potential is small (no more than 36 V) and the ions bombard the wall with just the energy gained in the low voltage sheath. Comparing all the probes (Table II), we see that the plasma potential was maintained very near the anode potential, the electron temperature was reduced by a factor of two to three, and the ion current density was reduced by at least a factor of two.

Figure 7 (left) shows an example of the centerline potential and temperature data for the US configuration. Our results are consistent with those measured by Reid and Gallimore on the H6 operating at the same conditions.^{26,27}

Similar to the wall probe data for the US configuration, the electron temperature peaks at 33 eV. The plasma potential is slightly above the 300 V anode potential deep in the channel, and falls to the coupling voltage a short distance downstream of the thruster exit plane. The centerline potential and temperature for the MS configuration are shown in Figure 7 (right). The electron temperature is also slightly higher (≈ 36 eV) and the axial temperature profile is not as narrow. The plasma potential is also just above the anode potential in the channel and extends to near the thruster exit plane. The shift in the electron temperature and plasma potential matched the shift downstream in the maximum magnetic field measured by a Gaussmeter (not shown).

B. Discharge chamber erosion

The carbon backscatter rate measured by the QCM was $4 \pm 1 \times 10^{-3} \mu\text{m/h}$. Within this uncertainty, the backscatter rate was independent of the thruster configuration. The rate measured in these experiments is on the order of backscatter rates measured in other Hall and gridded ion thruster experiments.^{29–32}

After testing each thruster configuration, erosion of the insulator rings was assessed through inspection of the surface conditions and wall profile measurements using the CMM. Erosion rates were calculated by dividing the change in radial dimension along the ring surface by the length of the testing window. The run time was calculated by summing the total energy expended during a testing window in units of kW-h and dividing by the nominal discharge power of 6 kW.³³ In this way, the startup transients and warm-up

TABLE II. Plasma parameters from the wall probes and calculated erosion rates at the wall for the US and MS configurations.

| Axial position (z/L_c) | Ion current density (mA/cm^2) | Electron temperature (eV) | Plasma potential relative to cathode (V) | Plasma potential relative to anode (V) | SEE yield (-) | Sheath potential (V) | Total ion energy | Ion incidence angle (degrees) | Sputter yield (mm^3/C) | Erosion rate ($\mu\text{m/h}$) |
|----------------------------------|--|---------------------------|--|--|---------------|----------------------|------------------|-------------------------------|--|----------------------------------|
| Unshielded-outer ring | | | | | | | | | | |
| 0.850 | 27 | 11.4 | 303.8 | 3.8 | 0.80 | -33.8 | 33.8 | 42 | 4.5E-05 | 0 |
| 0.893 | 17 | 28.1 | 236.3 | -63.7 | 1.00 | -28.7 | 92.4 | 42 | 1.6E-02 | 9.8 |
| 0.919 | 15 | 31.5 | 185.4 | -114.6 | 1.00 | -32.1 | 146.7 | 42 | 2.8E-02 | 15.6 |
| 0.947 | 14 | 30.8 | 154.8 | -145.2 | 1.00 | -31.4 | 176.6 | 42 | 3.3E-02 | 16.1 |
| 0.973 | 12 | 26.5 | 133.8 | -166.2 | 1.00 | -27.0 | 193.2 | 42 | 3.5E-02 | 15.0 |
| Unshielded-inner ring | | | | | | | | | | |
| 0.850 | 54 | 24.8 | 307.8 | 7.8 | 1.00 | -25.3 | 25.3 | 42 | 0 | 0 |
| 0.893 | 24 | 31.1 | 207.7 | -92.3 | 1.00 | -31.7 | 124.0 | 42 | 2.4E-02 | 20.3 |
| 0.919 | 21 | 32.3 | 189.8 | -110.2 | 1.00 | -32.9 | 143.1 | 42 | 2.8E-02 | 21.1 |
| 0.973 | 15 | 25.2 | 123.3 | -176.7 | 1.00 | -25.7 | 202.4 | 42 | 3.6E-02 | 19.7 |
| Magnetically shielded-outer ring | | | | | | | | | | |
| 0.746 | 25 | 6.1 | 304.1 | 4.0 | 0.68 | -21.0 | 21.0 | 0 | 0 | 0 |
| 0.846 | 12 | 6.7 | 307.2 | 7.1 | 0.70 | -22.9 | 22.9 | 0 | 0 | 0 |
| 0.846 | 11 | 7.1 | 308.9 | 8.8 | 0.70 | -23.9 | 23.9 | 0 | 0 | 0 |
| 0.893 | 9 | 8.3 | 310.6 | 10.5 | 0.73 | -27.2 | 27.2 | 0 | 0 | 0 |
| 0.947 | 5 | 9.3 | 310.2 | 10.1 | 0.75 | -29.7 | 29.7 | 0 | 0 | 0 |
| Magnetically shielded-inner ring | | | | | | | | | | |
| 0.746 | 15 | 6.2 | 304.7 | 4.6 | 0.68 | -21.3 | 21.3 | 0 | 0 | 0 |
| 0.846 | 7 | 7.0 | 309.4 | 9.3 | 0.70 | -23.6 | 23.6 | 0 | 0 | 0 |
| 0.893 | 8 | 10.2 | 316.1 | 16.0 | 0.77 | -31.6 | 31.6 | 0 | 0 | 0.0004 |
| 0.947 | 4 | 13.3 | 318.3 | 18.2 | 0.85 | -36.1 | 36.1 | 0 | 1.4E-04 | 0.02 |

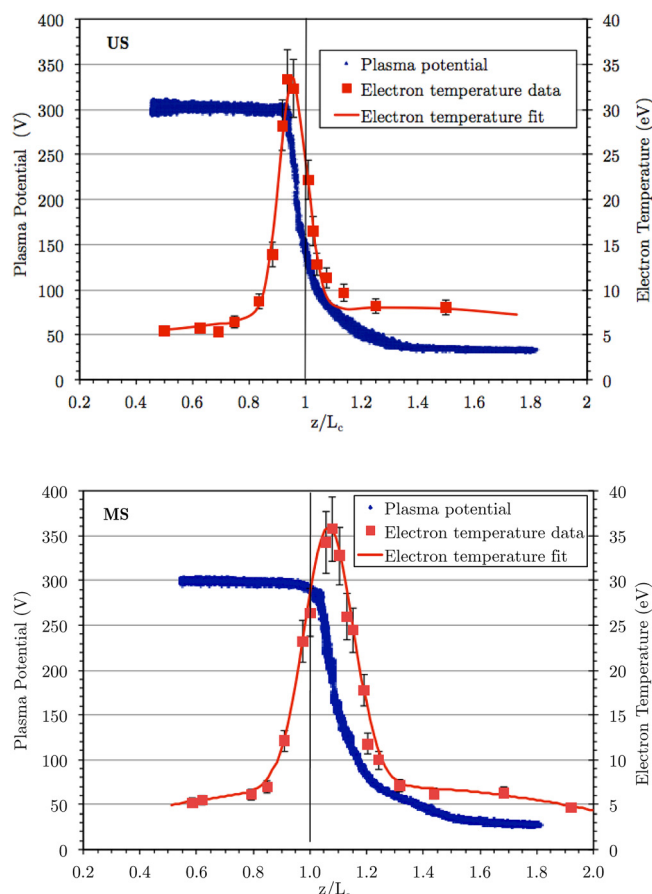


FIG. 7. Plasma potential (relative to cathode) and electron temperature measured on the channel centerline in the US (top) and MS (bottom) configurations. Parts of the data shown on the figures have been reprinted from Mikellides *et al.*, “Magnetic shielding of walls from the unmagnetized ion beam in a hall thruster,” *Appl. Phys. Lett.* **102**(2), 023509 (2013) Copyright American Institute of Physics.

periods when the thruster was not at 6 kW were accounted for. This correction relative to the absolute run time amounted to 6%–11% depending on the particular trial.

Photographs of the inner and outer insulator rings after testing in the US-A and MS-A configurations are shown in Figures 8 and 9, respectively. Side views of the inner rings for all four configurations tested are also shown in Figure 10. The surface of the US rings had portions showing evidence of net erosion and deposition, which is typical of unshielded Hall thrusters. The white color of the boron nitride is evident in the erosion zone, while a dark-brown film is present in the zone of net deposition that is composed of redeposited boron nitride from the erosion zone and carbon backspattered from the facility. When the erosion zone was viewed from the side the change in radial dimension due to erosion could be discerned by the human eye. The length of the erosion zone was symmetric around the circumference of the rings and was the same between the inner and outer rings. The erosion zone length in the US rings was measured to be $z/L_c = 0.13 \pm 0.01$.

In stark contrast to the US rings, the MS rings were covered in a conductive film that was dark grey to black in color from carbon backspattered from the vacuum chamber walls. Unlike the US rings, the dimensions of the MS rings appeared to be unchanged to the human eye. The film almost



FIG. 8. Inner rings after testing with the US (left) and MS (right) configurations. The plasma-exposed surface of the US rings had portions showing evidence of net erosion and deposition, while the plasma-exposed surface of the MS rings was almost entirely covered in a film of backspattered carbon.

uniformly covered both rings with the exception of a thin region on the inner ring with length $z/L_c = 0.03 \pm 0.01$ (Figure 10). This region showed evidence of net deposition due to discoloration of the white surface, but was still predominantly white. Subsequent testing determined that portions of the inner magnetic circuit were not completely seated against the back pole during the MS-A trial, which would have caused deviations in the magnetic field in the region where the inner ring was still mostly white. To test this hypothesis, the circuit was re-seated in the MS-B trial, and after the experiment the inner ring was uniformly covered by the carbon film (Figure 10).

In the MS configuration, field lines with high electron temperatures now terminate on the pole pieces, which were held at facility ground. This raises the possibility of significant electric fields being directed at the pole pieces, which could induce ion sputtering. However, the pole piece surfaces showed evidence of carbon deposition over most of their surfaces and there was no indication of significant sputtering. We hypothesize that the lack of sputtering in this region is due to the much lower plasma density that persists here, which will limit the flux to the surfaces. Additional investigations of this region are ongoing but are not expected to be a significant concern in flight applications.

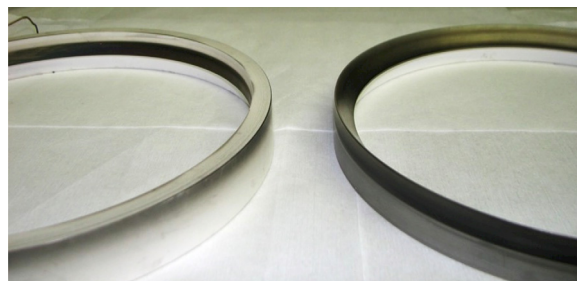


FIG. 9. Outer rings after testing with the US (left) and MS (right) configurations. The plasma-exposed surface of the US rings had portions showing evidence of net erosion and deposition, while the plasma-exposed surface of the MS rings was almost entirely covered in a film of backspattered carbon.

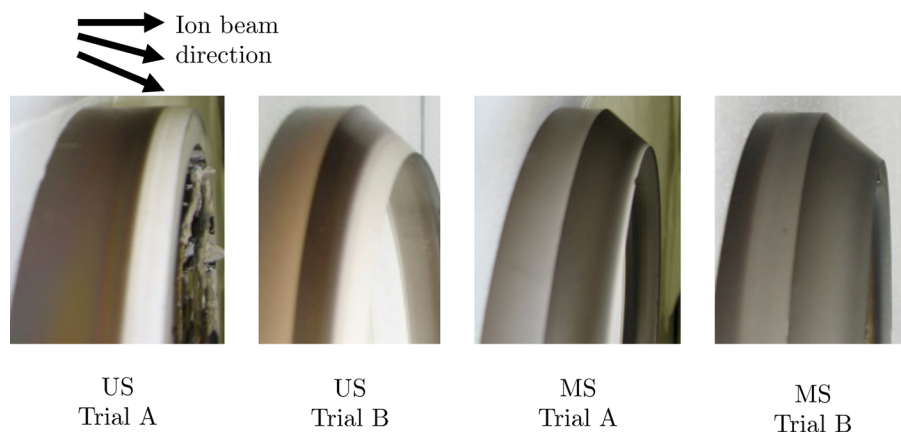


FIG. 10. Inner rings after testing for the various configurations described in Table I. The US trials displayed the characteristic zones of net deposition and erosion, while the MS trials resulted in net deposition from carbon backspattered from the vacuum chamber walls. The lack of an erosion zone in the MS trials was one indication that wall erosion had been significantly reduced relative to the US configuration.

The US-B trial tested the US magnetic circuit with the insulator ring geometry of the MS configuration. A side view of the inner ring from the US-B trial is shown in Figure 10. This trial was executed to demonstrate that chamfering was not the sole cause of the apparent reduction in erosion rate observed in the MS configuration. As expected, zones of erosion and deposition formed on the rings during testing that were very similar to the US-A trial (Figures 8–10). Numerical simulations (not shown) predict an erosion rate reduction by a factor of four for the US-B case relative to the US-A case, which is much less than the two to three orders of magnitude reductions that result when the magnetic field is configured for shielding. The length of the erosion zone was symmetric around the circumference of the rings and was the same between the inner and outer rings. The erosion zone length in the US-B rings was measured to be $z/L_c = 0.13 \pm 0.01$.

Erosion rates computed from the CMM measurements are shown in Figure 11 for the US-A and MS-A trials. For the US-A trials, measurements from segment 1 ($t = 7$ h) and segment 2 ($t = 28$ h) are shown. Positive values denote net erosion while negative values indicate deposition. The noise threshold of the CMM data is also indicated as the dashed lines at $\pm 1 \mu\text{m/h}$. For data below the threshold, only the sign of the erosion rate was judged to be significant. The carbon deposition rate measured by the QCM is also shown for reference.

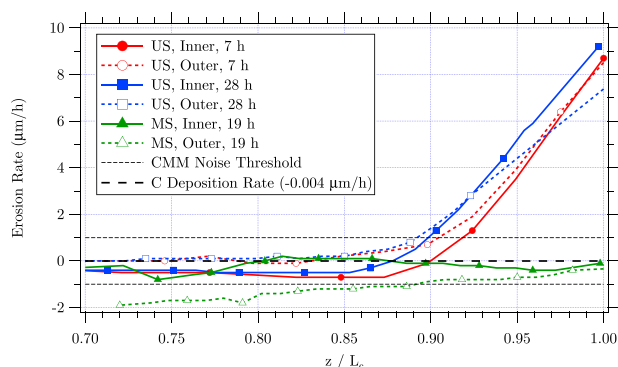


FIG. 11. Average erosion rate of the US and MS rings for various run times as measured by the CMM. The zone of net erosion for the US rings is consistent with the photographs shown in Fig. 10. Net deposition is indicated for the MS profiles, which is also consistent with Fig. 10. Parts of the data shown on the figure have been reprinted from Mikellides *et al.*, “Magnetic shielding of walls from the unmagnetized ion beam in a hall thruster,” *Appl. Phys. Lett.* **102**(2), 023509 (2013) Copyright American Institute of Physics.

The US erosion rates are consistent with the appearance of the rings where zones of net deposition and erosion were observed. Depending on the particular ring or time, the CMM show net erosion beginning around $z/L_c = 0.87 \pm 0.03$ on average. This is consistent with the value of 0.87 ± 0.01 measured directly from the rings marking the start of the erosion zone. The transition from erosion to deposition shifted slightly upstream from $t = 7$ h to 28 h. Small movements in the upstream boundary of the erosion zone are known to occur over time during long duration wear testing.⁵ The maximum erosion rate averaged over all rings and run times was $8.5 + 0.7/-1.0 \mu\text{m/h}$. Erosion rates of $5\text{--}10 \mu\text{m/h}$ are typical for unshielded Hall thrusters at beginning-of-life (BOL).^{5,34–44}

Net deposition is shown in Figure 11 for the MS rings over nearly the entire length of the rings. The outer ring deposition rate was measured to be greater than the CMM noise threshold at the upstream boundary, but the value was not judged to be accurate due to a systematic measurement bias in the data for this ring that added a constant slope to the data along the axial length. The bias was equivalent to only 0.16° of tilt. For both rings, the measured rates are at or near the CMM noise threshold and was interpreted as an indication that net deposition occurred with little if any change in the BOL dimensions of the MS rings. Discussed further below, these results imply that the erosion rate in the MS configuration decreased relative to the maximum, average erosion rates of the US configuration by orders of magnitude.

IV. DISCUSSION

Our results indicate that high performance was maintained in the magnetically shielded configuration while erosion rates were reduced by orders of magnitude. The reduction in erosion rates effectively eliminates discharge chamber erosion as the primary failure mode in Hall thrusters. Observations and quantitative measurements of the conditions at the walls in the magnetically shielded thruster consistently indicate that major reductions in the erosion rates occurred relative to the unshielded configuration, including (1) the plasma was observed to be in less contact with the wall during operation, (2) the MS rings were largely coated in a carbon film after testing, (3) the dimensions of the MS rings were unchanged after testing, (4) an experiment with an unshielded magnetic circuit and chamfered walls still developed an erosion zone, showing that chamfering was not

the sole cause for reduced erosion, (5) the MS rings operated at a temperature 60–80 °C less than the US rings, and, most importantly, (6) plasma measurements at the walls indicate that the plasma potential was maintained very near the anode potential, the electron temperature was reduced by a factor of two to three, and the ion current density was reduced by at least a factor of two. Below, we analyze the wall plasma measurements and demonstrate that these marked changes in properties led to conditions at the wall that reduced the erosion rate by orders of magnitude. We also discuss the relationship between the wall erosion and the backsputter rate of carbon.

Erosion of the channel walls results from sputtering of wall material caused by high-energy ion bombardment. The erosion rate is given by

$$\varepsilon = j_{i\perp} Y(K, \theta), \quad (1)$$

where $j_{i\perp}$ is the ion current density normal to the wall and Y is the sputtering yield of the wall material. The sputtering yield is a function of the energy K and angle of incidence θ of incoming ions. Ions obtain energy as they traverse the acceleration zone in the bulk plasma and through the negative wall sheath potential that develops to satisfy the zero net current condition at the insulating wall. For unshielded Hall thrusters operating at BOL, ions impact the wall at incidence angles typically less than 45° to the surface normal and erosion rates are high, on the order of 10 $\mu\text{m/h}$. As the wall erodes, the angle of incidence increases causing the ion current density to decrease and in turn the erosion rate. In modern Hall thrusters, the erosion can drop by a factor of 5 to 10 as the erosion proceeds, typically approaching 1 $\mu\text{m/h}$ near end-of-life (EOL).^{5,34–44} It is important to recognize that although the erosion rate drops by as much as an order of magnitude that the EOL rates are still high relative to walls that are typically just a few millimeters thick. At 1 $\mu\text{m/h}$, the wall is recessing 1 mm every 1000 h, so even if the thruster had a constant erosion rate of 1 $\mu\text{m/h}$, the life of a thruster with 10 mm thick walls would still only be 10 000 h. Lifetimes on the order of 10 000 h are on the low- to mid-end for deep-space missions, with many missions requiring 2–5 times more life. A capability then on the order of 100 000 h is needed to capture missions likely to be launched for the next several decades.

The erosion results from the CMM and visual deposition of backsputtered material can be compared against erosion rates calculated using the wall probe data. To do this, the electron temperature and plasma potential found from the wall probes embedded in the boron nitride rings were used to calculate the sheath potential and ion kinetic energy (from acceleration from the ionization region). Using the average impact angle determined by Shastry,²⁵ this provides an estimate of the total ion energy and angle for ions impinging on the rings. Using the ion flux from the probe and the sputtering yield for the estimated ion energy and angle,⁹ the total erosion rate at the wall was then calculated.

The sheath potential on the boron nitride surface depends on the electron temperature and the secondary electron emission (SEE) yield. The SEE yield up to the crossover energy E_1 (where the yield is unity) is given by⁴⁵

$$\gamma_e \approx \sigma_0 + (1 - \sigma_0) \frac{E_p}{E_1} = \sigma_0 + (1 - \sigma_0) \frac{2T_e}{E_1}, \quad (2)$$

where σ_0 is the effective yield at zero energy, E_p is the average electron energy which is equal to $2T_e$ for Maxwellian electrons.¹⁴ Values given in the literature for boron nitride are $\sigma_0 = 0.54$ and $E_1 = 40 \text{ eV}$.⁴⁵ The sheath potential for values of the SEE yield less than 0.983 (corresponding to electron temperatures less than 19.3 eV) is calculated based on the solution to the one-dimensional sheath equations in the presence of secondary electron emission provided by Hobbs and Wesson.⁴⁶ The sheath potential ϕ_s is given by¹⁴

$$\begin{aligned} \phi_s &= -\frac{kT_e}{e} \ln \left[\sqrt{\frac{m_{xe}}{2\pi m_e}} \frac{n_e}{n_e + n_s} \frac{v_B}{v_i} (1 - \gamma_e) \right] \\ &\approx -\frac{kT_e}{e} \ln \left[\sqrt{\frac{m_{xe}}{8\pi m_e}} (1 - \gamma_e) \right], \end{aligned} \quad (3)$$

which takes into account the secondary electron space charge n_s and finite ion temperatures in the ion velocity v_i . Here, m_{xe} and m_e are the xenon ion and electron mass, v_B is the Bohm velocity, and the rest of the symbols have their usual meaning. For electron temperatures above 19.3 eV, the sheath is space charge limited and the sheath potential is equal to $-1.02T_e$.⁴⁶

The ions arrive with an average incident angle θ and total impact energy of the ions at the wall is $K = K_i + \phi_s$, where K_i is the ion energy due to kinetic acceleration from the ionization region and ϕ_s is the sheath potential. The sputtering yield is determined using the fitting functions $f_K(K_i + \phi_s)$ for the energy dependence at zero angle of incidence, and $f_\theta(\theta)$ for the angle dependence as

$$\begin{aligned} Y(\theta, K) &= f_\theta(\theta) f_K(K), \\ f_\theta(\theta) &= \cos(\theta)^{-c_0} \exp \left[-c_1 \left(\frac{1}{\cos(\theta)} - 1 \right) \right], \\ f_K(K) &= c_2 \left[1 - \left(\frac{K_{th}}{K} \right)^{2/3} \right] \left(1 - \frac{K_{th}}{K} \right)^2. \end{aligned} \quad (4)$$

The coefficients for the angular- and energy-dependent functions are $c_0 = 7.19 \pm 4.04$, $c_1 = 5.40 \pm 3.43$, $c_2 = 0.053 \pm 0.002$, $K_{th} = 30.5 \pm 2.1 \text{ eV}$. The energy dependence is modeled after the functional form described by Bohdansky,⁴⁷ the angular dependence is modeled after Yamamura,⁴⁸ and the yields are from the measurements of low-energy sputtering by Rubin.⁴⁹ The sensitivity of our calculations on the fit coefficients, in particular the sputtering threshold, is discussed further in our companion paper.¹² Shastry²⁵ experimentally determined that the average incident angle for the ions coming into the wall probes in the unshielded configuration is about 42°. In the MS case, the ion energy is negligible and the incidence angle is zero degrees from the sheath acceleration.

Erosion rates calculated from the wall probe data decreased by orders of magnitude in the MS compared to the US configuration. This is shown in Table II, where the

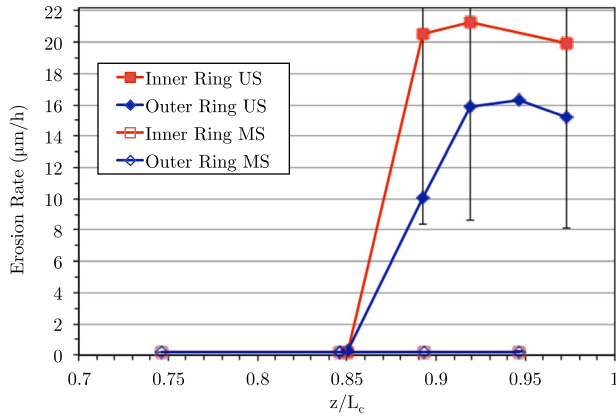


FIG. 12. Erosion rates calculated from the wall probe data for the US and MS configurations. Reductions greater than a factor of 1000 were computed. The result is independent of facility effects that may result from the finite backscatter rate of carbon.

wall-probe data and the calculated erosion rates from the inner and outer rings for the US and MS configurations are listed. The erosion rates are also plotted in Figure 12 as a function of the axial position in the channel. The uncertainty of the erosion rates calculated from the wall probe data is dominated by uncertainty in the ion current density (50%) and sputter yield (30%), resulting in a combined standard uncertainty of 60%. Within this uncertainty, the erosion rates computed from the US configuration probe data are consistent with the CMM data shown in Figure 11. In the MS case, the ion energies for most of the probes are below the 30.5 V sputtering threshold and thereby predict undetectable erosion rates. Non-zero erosion is calculated only for the last two probes on the inner wall where the electron temperature was between 10 and 13 eV, resulting in sheath potentials of 32–36 V. Sputtering for the last probe is consistent with the slightly lighter-colored coating of backspattered carbon observed in the MS configuration at the downstream tip of this ring (Figure 10). Still, the erosion rate at this location was reduced relative to the maximum rate calculated in the US configuration by more than a factor of 1000. Overall, the wall probe data provides erosion rate estimates consistent with the CMM data from the US configuration and suggests that the erosion rate for the MS configuration is orders of magnitude lower than the unshielded case. We also note that these calculations are independent of any facility effects that may result from the presence of backspattered carbon that are discussed later in this section.

The various rates encountered in this experiment and other wear tests of interest are illustrated in Figure 13. The H6US at BOL is near the top end of the scale at 9 $\mu\text{m/h}$, which falls in the expected range of 1–10 $\mu\text{m/h}$ for unshielded Hall thrusters over their service life.^{5,34–44} Erosion diagnostics in use in the electric propulsion community are approximately capable of resolving rates as low as 0.01–1 $\mu\text{m/h}$, with the CMM used here having a noise floor of 1 $\mu\text{m/h}$. At the onset of these experiments, it was clear that the predicted erosion rates would be much lower than existing diagnostics in the community. This became another motivation for the wall

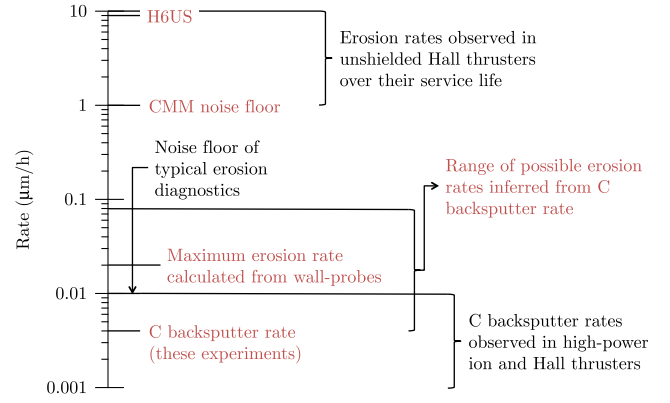


FIG. 13. Illustration of the various rates encountered in these experiments (red) and other relevant cases. The noise floor of existing erosion diagnostics and carbon backscatter rate are near the rates encountered in magnetically-shielded Hall thrusters. However, calculations from direct measurements of the plasma properties, which are independent of these considerations, indicate that the erosion rates of the MS configuration were reduced by a factor of 1000 relative to the US configuration and a factor of 100 relative to unshielded Hall thrusters late in life.

probe measurements, since knowing the plasma conditions at the wall would provide the opportunity to compute the erosion rates independent of facility effects that may result from the carbon backscatter rate. An approximate range of carbon backscatter rates observed in high-power Hall and Ion thruster testing of 0.001–0.01 $\mu\text{m/h}$ is also indicated,^{29–32} along with the 0.004 $\mu\text{m/h}$ rate measured in these experiments.

In these experiments, net deposition of carbon (C) was observed in the MS configuration. However, observing net deposition does not necessarily establish the upper limit of the erosion rate as the backscatter rate. This is because carbon is being deposited and sputtered at the wall. Under conditions where there is net deposition of carbon, the erosion rate is reduced and this reduction depends on several factors, most critically, the ratio of sputter yields of the BN wall material and carbon. The actual erosion rate due to xenon bombardment on BN, that is, the erosion rate that would persist if the carbon backscatter rate R_c were zero, is given by

$$\varepsilon_{Xe-BN} \leq \alpha R_c \frac{\rho_C m_{BN}}{\rho_{BN} m_C} \frac{Y_{Xe-BN}}{Y_{Xe-C/BN}} \approx 2 R_c \frac{Y_{Xe-BN}}{Y_{Xe-C/BN}}, \quad (5)$$

if the sticking coefficient (α) is unity. Here, ρ , m , and Y are the density, mass, and sputter yield of the materials of interest. Equation (5) establishes an upper bound on the erosion rate that is dependent on the sputtering yield ratio. If the yield ratio is of order unity, the measured carbon backscatter rate may be used to establish a maximum for the BN erosion rate. When the yield ratio is greater than one, the maximum BN erosion rate could be greater than the backscatter rate, but it could also be much less. This is an indeterminate case that could span orders of magnitude in our estimate of the BN erosion rate. Thus, the BN to C/BN yield ratio is a critical parameter in our interpretation of the MS rings becoming coated with a film.

Estimating the sputtering yield ratio in Eq. (5) is complicated by several factors. First, while the carbon sputtering yield by xenon bombardment has been measured down to

energies of 50 eV, deposited carbon on BN should be amorphous and this sputtering yield is unknown. Since the conservative approach is to assume that the yields of amorphous and crystalline carbon are identical, we will set aside this consideration. Second, sputtering yields for BN and C have only been measured down to ion energies of 60 and 50 eV,^{49,50} respectively, yet the sheath potentials in the MS case were no greater than 36 V. The sputtering thresholds of BN and C are uncertain in this energy range. Our review of the literature indicates that the sputtering thresholds for BN and C are in the range of 25–50 eV.^{25,35,49,51–56} Near threshold, the shape and magnitude of the yield function changes by orders of magnitude over just a few electron volts, so knowledge of this yield ratio is highly uncertain. If we examine the yield ratio based on the known data over the energy range of 50–200 V, the ratio is of order one to ten. What guidance this really provides though is unclear considering that below 50 V, the yields are rapidly plummeting. Still, the most conservative approach would be to assume that a ratio as high as ten is valid even near threshold. Using Eq. (5), this would result in a maximum erosion rate for the MS configuration of 0.08 $\mu\text{m/h}$ ($0.004 \times 2 \times 10$). If however, the BN threshold is greater than the 36 V maximum sheath potential that was measured, the yield ratio is zero and the backsputter rate can be used to establish an upper limit on the BN erosion rate. This places the erosion rate, based solely on the measured backsputter rate of carbon, in the range of 0.004–0.08 $\mu\text{m/h}$, or expressed in terms of the maximum US erosion rate, a reduction in the MS erosion rate relative to the US case by a factor of 100–2000.

In addition, we note that the uncertainty in the sputtering yield ratio is potentially resolvable, even if the ratio is never rigorously measured. If the BN wall material were replaced with carbon, the yield ratio would be unity. In this case, and provided an experiment resulted in net deposition with no change in the wall dimensions, one could confidently estimate the erosion rate of a carbon-walled Hall thruster to be no greater than the backsputter rate. Experiments to consider precisely this situation will be reported in the near future.

Estimates of the erosion rate reduction deduced from the measured carbon backsputter rate range from 100 to 2000, while reductions calculated from the wall probe data indicate a reduction by a factor of 1000. The wall probe rates are taken as a more accurate estimate of the reductions possible with magnetic shielding since they are independent of any facility effects and still fall within our estimates based on the backsputter rate. The factor of 1000 reduction relative to the US erosion rate is a BOL rate, however, so a more relevant comparison may be rates observed near EOL in unshielded thrusters. Typically, up to a factor of 10 reduction is measured,^{5,34–44} so the MS reduction relative to late in life Hall thrusters is estimated to be a factor of 100. Since unshielded Hall thrusters are typically capable of 1–10 kh of operation, this places the lifetime of a magnetically shielded Hall thruster on the order of 100–1000 kh. The life estimates provided here are at least a factor of 100 greater than existing capability and even for the most ambitious deep-space missions presently being considered, still greater than by a factor

of 20. Such extraordinary capabilities effectively eliminate wall erosion as a practical consideration in Hall thrusters.

V. CONCLUSION

Experiments were performed comparing the performance, thermal, stability, and wear characteristics of a magnetically shielded Hall thruster relative to an unshielded configuration. The primary goal of the experiments was to validate the physics of magnetic shielding first identified through numerical simulation and subsequently applied to the present design modifications. It was also desired to validate the physics-based methodology used to design the thruster while still maintaining the performance benefits of a plasma lens magnetic field topology. The results of these experiments all indicate that these objectives have been met and that the experimental validation of magnetic shielding physics is complete.

Our results show that practically erosion-free operation has been achieved in a high-performance Hall thruster. Total efficiency decreased by only 1.7% while specific impulse increased by 2.9%. The temperatures of the insulator rings were reduced by 12%–16%. Discharge current oscillations, while increasing 25%, did not affect the global stability of the discharge. Most importantly, multiple diagnostics and analysis were used to assess the relative wear rates of the different configurations and it was shown that a factor of 1000 reduction was achieved relative to the US configuration, or, expressed relative to unshielded Hall thrusters at EOL a factor of 100 decrease was achieved.

The implications of our results for the future of Hall thruster design and the infusion of this technology on deep-space missions are significant. By simultaneously achieving high-performance and long-life, the mission capture for Hall thrusters essentially increases to most, if not all, SEP missions for the next several decades. Unlike unshielded thrusters that experience minor but non-negligible performance variations, removing time-dependent geometry changes of the discharge chamber should result in nearly constant performance over tens of thousands of hours. Further, magnetic shielding potentially reduces the cost and schedule risk of qualifying new thruster designs by several million dollars since verifying new designs that exhibit negligible wear would be very inexpensive. The extremely low erosion rates reported here places new emphasis on our understanding of surface physics in Hall thruster discharge chambers, as well as a strong need to develop high sensitivity erosion diagnostics that may be practically implemented in the context of a thruster qualification program.

Finally, magnetic shielding opens up new possibilities in thruster design. Our findings strongly suggest that plasma-wall interactions have been significantly reduced, perhaps even made negligible. This opens the trade space to possibly achieving wide throttling and high-performance simultaneously with long-life. High power density operation should also be possible, which could lead to compact thrusters with specific masses two to three times lower than current capabilities. Reduced or eliminated plasma-wall interactions beg the question of whether the wall material is relevant in

magnetically shielded Hall thrusters. Replacing the relatively fragile and expensive boron nitride walls with alternate materials such as carbon would be a path towards a low-cost, structurally robust propulsion system that should be especially advantageous at high power where the fragility of ceramics makes the fabrication of large Hall thrusters capable of surviving launch loads a challenging engineering endeavor. All told, these experiments have provided exciting new avenues to explore in Hall thruster design. The magnitude of the changes in erosion rate deduced from these experiments effectively eliminates wall erosion as a life limitation or failure mode in Hall thrusters. When these systems are brought to flight-status, the door to the robotic and human exploration of the solar system will be opened much wider.

ACKNOWLEDGMENTS

The research described in this paper was carried out at the Jet Propulsion Laboratory, California Institute of Technology, under a contract with the National Aeronautics and Space Administration and funded through the internal Research and Technology Development program. The authors are indebted to Al Owens and Ray Swindlehurst for their assistance throughout the test campaign constructing and implementing the test apparatus and maintaining the vacuum facility. Thanks also to David Conroy, Brandon Dotson, and James Polk for their insight and contributions with the magnetic field, temperature, and erosion diagnostics.

- ¹R. R. Hofer and A. D. Gallimore, *J. Propul. Power* **22**(4), 721–731 (2006).
- ²R. R. Hofer and A. D. Gallimore, *J. Propul. Power* **22**(4), 732–740 (2006).
- ³A. I. Morozov, *Sov. Phys. Dokl.* **10**(8), 775–777 (1966).
- ⁴A. I. Morozov and V. V. Savelyev, in *Reviews of Plasma Physics*, edited by B. B. Kadomtsev and V. D. Shafranov (Consultants Bureau, New York, 2000), Vol. 21, pp. 203–390.
- ⁵K. H. de Grys, A. Mathers, B. Welander, and V. Khayms, AIAA Paper 2010–6698, 2010.
- ⁶I. G. Mikellides, I. Katz, R. R. Hofer, D. M. Goebel, K. H. De Grys, and A. Mathers, *Phys. Plasmas* **18**, 033501 (2011).
- ⁷I. G. Mikellides and I. Katz, *Phys. Rev. E* **86**(4), 046703 (2012).
- ⁸I. G. Mikellides, I. Katz, and R. R. Hofer, AIAA Paper 2011–5809, 2011.
- ⁹I. G. Mikellides, I. Katz, R. R. Hofer, and D. M. Goebel, AIAA Paper 2012–3789, 2012.
- ¹⁰R. R. Hofer, D. M. Goebel, I. G. Mikellides, and I. Katz, AIAA Paper 2012–3788, 2012.
- ¹¹I. G. Mikellides, I. Katz, R. R. Hofer, and D. M. Goebel, *Appl. Phys. Lett.* **102**(2), 023509 (2013).
- ¹²I. G. Mikellides, I. Katz, R. R. Hofer, and D. M. Goebel, *J. Appl. Phys.* **115**, 043303 (2014).
- ¹³V. V. Zhurin, H. R. Kaufman, and R. S. Robinson, *Plasma Sources Sci. Technol.* **8**(1), R1–R20 (1999).
- ¹⁴D. M. Goebel and I. Katz, *Fundamentals of Electric Propulsion: Ion and Hall Thrusters* (John Wiley & Sons, New York, 2008).
- ¹⁵J. M. Haas, R. R. Hofer, D. L. Brown, B. M. Reid, and A. D. Gallimore, in Proceedings of the 54th JANNAF Propulsion Meeting, Denver, CO, 14–17 May 2007.
- ¹⁶D. L. Brown, C. W. Larson, B. E. Beal, and A. D. Gallimore, *J. Propul. Power* **25**(6), 1163–1177 (2009).
- ¹⁷B. M. Reid, A. D. Gallimore, R. R. Hofer, Y. Li, and J. M. Haas, JANNAF J. Propul. Energ. **3**(1), 29–43 (2010).
- ¹⁸W. Huang, A. D. Gallimore, and R. R. Hofer, *J. Propul. Power* **27**(3), 553–563 (2011).
- ¹⁹R. R. Hofer, D. M. Goebel, and R. M. Watkins, U.S. patent 8,143,788 (27 March 2012).
- ²⁰D. M. Goebel, K. K. Jameson, and R. R. Hofer, *J. Propul. Power* **28**(2), 355–363 (2012).
- ²¹R. R. Hofer, U.S. patent 8,407,979 (2 April 2013).
- ²²R. R. Hofer, Ph.D. dissertation, University of Michigan, 2004.
- ²³R. R. Hofer, L. K. Johnson, D. M. Goebel, and R. E. Wirz, *IEEE Trans. Plasma Sci.* **36**(5), 2004–2014 (2008).
- ²⁴R. Shastry, A. D. Gallimore, and R. R. Hofer, AIAA Paper 2011–5589, 2011.
- ²⁵R. Shastry, Ph.D. dissertation, University of Michigan, 2011.
- ²⁶B. M. Reid and A. D. Gallimore, AIAA Paper 2008–5185, 2008.
- ²⁷B. M. Reid and A. D. Gallimore, AIAA Paper 2008–4920, 2008.
- ²⁸A. Fruchtman, D. Zoler, and G. Makrinich, *Phys. Rev. E* **84**(2), 025402 (2011).
- ²⁹T. Randolph, V. Kim, H. Kaufman, K. Kozubsky, V. Zhurin, and M. Day, in Proceedings of the 23rd International Electric Propulsion Conference, IEPC Paper 1993-093, Seattle, WA, 13–16 September 1993.
- ³⁰J. Kahn, V. Zhurin, K. Kozubsky, T. Randolph, and V. Kim, in *Proceedings of the 23rd International Electric Propulsion Conference, IEPC-93-092, Seattle, WA, 13–16 September 1993*.
- ³¹J. E. Polk, O. B. Duchemin, C. Ho, and B. E. Koel, AIAA Paper 2000–3662, 2000.
- ³²J. L. Van Noord and G. C. Soulas, AIAA Paper 2005–4067, 2005.
- ³³R. R. Hofer, AIAA Paper 2010–6623, 2010.
- ³⁴S. K. Absalamov, V. B. Andreev, T. Colbert, M. Day, V. V. Egorov, R. U. Gnizdor, H. Kaufman, V. Kim, A. I. Korakin, K. N. Kozubsky, S. S. Kudravyev, U. V. Lebedev, G. A. Popov, and V. V. Zhurin, AIAA Paper 1992–3156, 1992.
- ³⁵V. Abgaryan, H. R. Kaufman, V. Kim, D. Ovsyanko, I. Shkarban, A. Semenov, A. Sorokin, and V. Zhurin, AIAA Paper 94–2859, 1994.
- ³⁶C. E. Garner, J. R. Brophy, J. E. Polk, and L. C. Pless, AIAA Paper 94–2856, 1994.
- ³⁷B. A. Arkhipov, A. S. Bober, R. Y. Gnizdor, K. N. Kozubsky, A. I. Korakin, N. A. Maslenikov, and S. Y. Pridannikov, in Proceedings of the 24th International Electric Propulsion Conference, IEPC Paper 1995-039, Moscow, Russia, 19–23 September, 1995.
- ³⁸C. E. Garner, J. R. Brophy, J. E. Polk, and L. C. Pless, AIAA Paper 95–2667, 1995.
- ³⁹V. Petrosov, A. I. Vasin, V. I. Baranov, J. R. Wetch, E. J. Britt, S. P. Wong, and R. Lin, in Proceedings of the 24th International Electric Propulsion Conference, IEPC-95-41, Moscow, Russia, 19–23 September, 1995.
- ⁴⁰R. Gnizdor, K. Kozubsky, A. Koryakin, N. Maslenikov, S. Pridannikov, and M. Day, AIAA Paper 1998–3790, 1998.
- ⁴¹L. S. Mason, R. S. Jankovsky, and D. H. Manzella, AIAA Paper 2001–3773, 2001.
- ⁴²F. R. Marchandise, J. Biron, M. Gambon, N. Cornu, F. Darnon, and D. Estublier, in Proceedings of the 29th International Electric Propulsion Conference, IEPC Paper 2005-209, Princeton, NJ, 31 October to 4 November 2005.
- ⁴³P. Y. Peterson, D. T. Jacobson, D. H. Manzella, and J. W. John, AIAA Paper 2005–4243, 2005.
- ⁴⁴N. Cornu, F. Marchandise, F. Darnon, and D. Estublier, AIAA Paper 2007–5197, 2007.
- ⁴⁵A. Dunaevsky, Y. Raites, and N. J. Fisch, *Phys. Plasmas* **10**(6), 2574–2577 (2003).
- ⁴⁶G. D. Hobbs and J. A. Wesson, *Plasma Phys.* **9**, 85–87 (1967).
- ⁴⁷J. Bohdansky, *Nucl. Instrum. Methods Phys. Res. B* **2**(1–3), 587–591 (1984).
- ⁴⁸Y. Yamamura and S. Shindo, *Radiat. Eff.* **80**(1–2), 57–72 (1984).
- ⁴⁹B. Rubin, J. L. Topper, and A. P. Yalin, *J. Phys. D: Appl. Phys.* **42**(20), 205205 (2009).
- ⁵⁰R. P. Doerner, D. G. Whyte, and D. M. Goebel, *J. Appl. Phys.* **93**(9), 5816–5823 (2003).
- ⁵¹E. J. Pencil, T. Randolph, and D. H. Manzella, AIAA Paper 1996–2709, 1996.
- ⁵²Y. Garnier, V. Viel, J. F. Roussel, and J. Bernard, *J. Vac. Sci. Technol. A* **17**(6), 3246–3254 (1999).
- ⁵³V. Kim, V. Kozlov, A. Semenov, and I. Shkarban, in Proceedings of the 27th International Electric Propulsion Conference, IEPC Paper 2001-073, Pasadena, CA, 15–19 October 2001.
- ⁵⁴R. R. Hofer, I. G. Mikellides, I. Katz, and D. M. Goebel, in Proceedings of the 30th International Electric Propulsion Conference, IEPC Paper 2007–267, Florence, Italy, 17–20 September 2007.
- ⁵⁵S. Y. Cheng and M. Martinez-Sanchez, *J. Propul. Power* **24**(5), 987–998 (2008).
- ⁵⁶J. T. Yim, Ph.D. dissertation, University of Michigan, 2008.